

# Journal of Materials Chemistry C

Materials for optical, magnetic and electronic devices

Accepted Manuscript

This article can be cited before page numbers have been issued, to do this please use: J. Necib, E. Feldbach, I. Romet, V. Nagirnyi, I. Hussainova, T. Jüstel and R. E. Rojas Hernandez, *J. Mater. Chem. C*, 2026, DOI: 10.1039/D6TC00560H.



This is an Accepted Manuscript, which has been through the Royal Society of Chemistry peer review process and has been accepted for publication.

Accepted Manuscripts are published online shortly after acceptance, before technical editing, formatting and proof reading. Using this free service, authors can make their results available to the community, in citable form, before we publish the edited article. We will replace this Accepted Manuscript with the edited and formatted Advance Article as soon as it is available.

You can find more information about Accepted Manuscripts in the [Information for Authors](#).

Please note that technical editing may introduce minor changes to the text and/or graphics, which may alter content. The journal's standard [Terms & Conditions](#) and the [Ethical guidelines](#) still apply. In no event shall the Royal Society of Chemistry be held responsible for any errors or omissions in this Accepted Manuscript or any consequences arising from the use of any information it contains.

# Molten Salt–Assisted Screen Printing of Highly Textured Zn<sub>2</sub>SiO<sub>4</sub> Films with Enhanced Deep UV Emission

Jallouli Necib\*<sup>1</sup>, Eduard Feldbach<sup>2</sup>, Ivo Romet<sup>2</sup>, Vitali Nagirnyi<sup>2</sup>, Irina Hussainova<sup>1</sup>, Thomas Jüstel<sup>3</sup>, and Rocío E. Rojas-Hernandez<sup>1,4</sup>

<sup>1</sup> Department of Mechanical and Industrial Engineering, Tallinn University of Technology, Ehitajate 5, 19180 Tallinn, Estonia

<sup>2</sup> Institute of Physics, University of Tartu, W. Ostwald Str 1, 50411 Tartu, Estonia

<sup>3</sup> FH Münster University of Applied Sciences, Department of Chemical Engineering, Stegerwaldstr. 39, D-48565, Steinfurt, Germany

<sup>4</sup> Electroceramic Department, Instituto de Cerámica y Vidrio, CSIC, Kelsen 5, 28049, Madrid, Spain

## Abstract

A novel and scalable approach for the fabrication of deep ultraviolet (UV) emitting materials is presented through the synthesis of highly textured zinc silicate films using screen printing assisted by a NaCl-KCl eutectic flux. This work provides the first demonstration of intrinsic deep UV emission in screen-printed Zn<sub>2</sub>SiO<sub>4</sub> films and establishes a correlation between processing conditions, interfacial phase evolution, and optical response. The films exhibited strong preferential orientation along the (300) plane with Lotgering factors reaching up to 0.94. Interface analysis reveals the pivotal role of flux-mediated phase transformations in governing film growth dynamics and surface morphology. Detailed luminescence studies identified intense deep UV emission at 4.43 eV (280 nm), attributed to intrinsic electronic transitions within the Zn<sub>2</sub>SiO<sub>4</sub> material. Synchrotron radiation studies indicate that the emission involves band-to-band transitions and excitonic processes influenced by the local structural environment. Notably, emission intensity correlates strongly with both crystallographic texturing and the quality of the film-substrate interface, highlighting the key role of interface and structural control in enhancing deep UV emission. The demonstrated method offers a promising pathway for the development of mercury-free and rare-earth-free deep UV emitters for next-generation photonic and optoelectronic applications.



31 **Keywords:** Zn<sub>2</sub>SiO<sub>4</sub> films; Molten salt synthesis; Screen-printing; Crystallographic texturing;  
32 Interface engineering; Deep UV emission; Synchrotron radiation spectroscopy; Heavy-metal-  
33 and Rare-earth-free phosphors.

## 34 1. Introduction

35 The demand for deep ultraviolet (UV) emitters, particularly in the UV-C (100-280 nm) and  
36 UV-B (280-315 nm) spectral ranges, has surged in recent years owing to their critical  
37 applications in disinfection, medicine, and agriculture<sup>1-9</sup>. Recent epidemics have further  
38 underscored the importance of UV-C radiation for pathogen inactivation<sup>1,2</sup>, highlighting the  
39 urgent need for efficient and sustainable deep UV light sources. However, the conventional  
40 deep UV emitters such as mercury lamps pose significant environmental and health risks,  
41 leading to global initiatives such as the Minamata convention on mercury to phase out their  
42 use<sup>10</sup>. Although rare-earth-doped phosphors have been explored as alternatives, their  
43 dependence on rare-earth elements presents challenges related to resource availability, cost,  
44 and geopolitical constraints<sup>11,12</sup>.

45 In parallel, deep UV emission has been extensively developed in wide band gap semiconductor  
46 systems, particularly AlN and AlGaIn alloys, which represent the leading solid-state platform  
47 for deep UV light sources<sup>13-15</sup>. However, only a limited number of materials are known to  
48 exhibit efficient deep UV emission<sup>16,17</sup>, indicating a restricted materials space in this spectral  
49 range. Recent high-throughput computational studies further support this observation by  
50 identifying only a small group of rare-earth-free wide band gap compounds with suitable  
51 electronic structures for deep UV emission, such as BeGeN<sub>2</sub>, Mg<sub>3</sub>NF<sub>3</sub>, and KCaBr<sub>3</sub><sup>17</sup>.

52 Within this framework, selected oxide materials have emerged as promising candidates for  
53 deep UV emission, where luminescence arises from intrinsic electronic transitions that are  
54 strongly influenced by local structural and defect environments, making precise control over  
55 crystallization and defect formation essential for optimizing emission efficiency<sup>18,19</sup>. This  
56 structure-sensitive behaviour is exemplified by ZnAl<sub>2</sub>O<sub>4</sub>, where deep UV emission has been  
57 linked to excitons perturbed by oxygen vacancies<sup>20,21</sup>. Other wide band gap oxides, including  
58 ZnGa<sub>2</sub>O<sub>4</sub> and K<sub>2</sub>ZrSi<sub>2</sub>O<sub>7</sub>, have also demonstrated intrinsic deep UV emission<sup>22,23</sup>, illustrating  
59 the capability of these materials to function as rare earth free emitters. Among these materials,  
60 zinc silicate (Zn<sub>2</sub>SiO<sub>4</sub>), with a band gap width ranging from 5.5 to 6.26 eV according to  
61 different studies<sup>24-27</sup>, has gained attention because of its potential for intrinsic deep UV  
62 luminescence. While most studies have been focused on doped Zn<sub>2</sub>SiO<sub>4</sub> for visible emission,



63 its undoped form remains largely unexplored for UV applications. In our previous  
64 investigations, undoped  $\text{Zn}_2\text{SiO}_4$  powders synthesized via sol-gel and molten salt routes  
65 exhibited intrinsic UV-B emission<sup>28,29</sup>, demonstrating the potential of  $\text{Zn}_2\text{SiO}_4$  as a rare-earth-  
66 free deep UV emitter. However, the extension of this intrinsic emission behaviour to film form  
67 remains limited. The prior studies have been primarily focused on nanocables, nanotubes, or  
68 sputtered films<sup>30-33</sup>. For example, Furukawa et al.<sup>33</sup> reported a 300 nm emission band in  
69  $\text{Zn}_2\text{SiO}_4$  thin films synthesized via radio frequency magnetron sputtering, whereas Peng et al.<sup>34</sup>  
70 observed no detectable photoluminescence under similar conditions, illustrating the challenges  
71 in achieving consistent deep UV emission. These contrasting results clearly indicate a need for  
72 research aimed at understanding how processing conditions, phase evolution, and interfacial  
73 reactions govern intrinsic luminescence in  $\text{Zn}_2\text{SiO}_4$  films. Moreover, the complexity, high  
74 energy demand, and cost of sputtering techniques further limit their practical application.

75 In contrast, solution-based techniques such as screen printing offer a simple, scalable, cost-  
76 effective, and environmentally friendly alternative<sup>35-37</sup>. Unlike vacuum-based deposition  
77 methods, screen printing allows for straightforward fabrication under ambient conditions while  
78 also enabling control over film morphology<sup>37</sup>. A related area of interest concerns the influence  
79 of film texturing. Textured films have been shown to have improved luminescent properties.  
80 For example, highly textured  $\text{Zn}_2\text{SiO}_4:\text{Mn}^{2+}$  phosphor films exhibited a photoluminescence  
81 brightness of 65% relative to a commercially available  $\text{Zn}_2\text{SiO}_4:\text{Mn}^{2+}$  phosphor powder<sup>38</sup>.

82 This study presents a novel strategy for the synthesis of textured  $\text{Zn}_2\text{SiO}_4$  films using screen  
83 printing assisted by a molten salt flux. By optimizing the ink formulation and using a single-  
84 crystal  $\text{SiO}_2$  substrate, the highly textured  $\text{Zn}_2\text{SiO}_4$  films with a pronounced preferential  
85 orientation along the (300) plane were fabricated. These films exhibited an intrinsic deep UV  
86 emission attributed to excitonic processes within the host lattice. Additionally, a green emission  
87 band was observed, likely originating from trace  $\text{Mn}^{2+}$  impurity. To the best of our knowledge,  
88 this study is the first to report deep UV emission from screen-printed  $\text{Zn}_2\text{SiO}_4$  films, offering  
89 a rare-earth- and heavy metal-free solution for next-generation UV devices with a simple,  
90 scalable, and efficient fabrication process.

## 91 2. Experimental Section

### 92 2.1. Film preparation

93 A series of inks was formulated with varying  $\text{ZnO}/\text{SiO}_2$  ratios (0.5Zn, 1.0Zn, 1.5Zn, and 2.0Zn  
94 relative to the nominal 2.0ZnO:1.0SiO<sub>2</sub> stoichiometry), each incorporating an eutectic mixture



95 of 0.5NaCl-0.5KCl in a consistent 3:1 ratio relative to ZnO. The inks were prepared by mixing  
96 ZnO (Symrise GmbH) with the eutectic salt mixture and an organic vehicle. The composition  
97 of the organic vehicle has been described in detail elsewhere<sup>37</sup>. The mixture was homogenized  
98 in a planetary ball mill (Model YKM-1) using yttria-stabilized zirconia (YSZ) balls in 250 ml  
99 zirconia jars at 250 rpm for 8 h. To ensure optimal consistency, the ink was further processed  
100 in a three-roll mill (Dermamill 100SP Ointment Mill) with a 10 μm gap and a rotation speed  
101 of 25 rpm. This process was repeated three times to achieve a homogeneous ink.

102 The prepared ink was screen-printed onto single-side polished single-crystal quartz substrates  
103 (SiO<sub>2</sub> (0001), Biotain Crystal Co.) using a JM322R screen-printing device (Zhuhai Kaivo  
104 Optoelectronic Technology Co., Ltd). After deposition, a multi-step drying procedure was  
105 employed to remove the organic vehicle. The samples were heated at a controlled rate of 0.5  
106 °C/min across temperatures of 150, 195, 270, 386, and 425 °C. Final thermal treatments were  
107 conducted at 1100 and 1200 °C in air for 4 h to ensure complete removal of the eutectic salt  
108 mixture, with heating and cooling rates of 5 °C/min.

## 109 2.2. Characterization

110 The phase composition of the synthesized Zn<sub>2</sub>SiO<sub>4</sub> films was investigated using X-ray  
111 diffraction (XRD) on a Rigaku SmartLab SE diffractometer equipped with a D/teX Ultra 250  
112 1D detector. Measurements were performed in a Bragg-Brentano configuration with Cu Kα  
113 radiation, scanning a 2θ range of 10-80°. The degree of preferred orientation in the films was  
114 quantified using the Lotgering factor (LF) calculated as follows<sup>39</sup>:

$$115 \quad LF = \frac{P - P_0}{1 - P_0}, \quad P = \frac{\sum I_{(00l)}}{\sum I_{(hkl)}}, \quad P_0 = \frac{\sum I_{0(00l)}}{\sum I_{0(hkl)}} \quad (1)$$

116 Here, I and I<sub>0</sub> represent the intensities of the diffraction peaks for the textured and randomly  
117 oriented samples, respectively. LF ranges from 0 to 1, where 0 indicates a random orientation  
118 and 1 corresponds to perfect alignment along the preferred growth direction.

119 The average crystallite size (D) was calculated using the Scherrer's formula<sup>40</sup>:

$$120 \quad D = \frac{k\lambda}{\beta \cos \theta} \quad (2)$$

121 where, k is a form factor (0.9), λ is the wavelength of the Cu Kα radiation (1.54060 Å), β is  
122 peak broadening after instrumental correction (in radians), and θ is the Bragg diffraction angle.



123 The surface morphology and microstructure of the films were examined using field-emission  
124 scanning electron microscopy (FE-SEM, Zeiss ULTRA-55) equipped with energy dispersive  
125 X ray spectroscopy (EDS, Bruker Esprit 1.82 system) for elemental analysis.

126 Confocal Raman microscopy was performed using a WITEC Alpha 300R system equipped  
127 with a 532 nm excitation laser and a 100x objective lens (NA = 0.9) at an incident laser power  
128 of 0.5 mW. The optical diffraction resolution of the system was approximately 200 nm laterally  
129 and 500 nm vertically, with a spectral resolution of 0.02  $\text{cm}^{-1}$ . Samples were mounted on a  
130 piezo-driven scan platform, enabling precise positioning with 4 nm lateral and 0.5  $\mu\text{m}$  vertical  
131 accuracy. Raman spectra were collected and processed using Witec Control Plus software to  
132 identify phase transformations and chemical interactions at the film-substrate interface.

133 The luminescent properties of  $\text{Zn}_2\text{SiO}_4$  films were investigated using X-ray excited optical  
134 luminescence (XEOL), cathodoluminescence (CL), and synchrotron radiation-excited  
135 photoluminescence. XEOL measurements were conducted using an Edinburgh Instruments  
136 FLS980 spectrometer equipped with a Hamamatsu R298P photomultiplier and an X-ray tube  
137 (Oxford Instruments Neptune 5200) operating at 10-50 kV. CL analysis was performed using  
138 an electron beam with an energy of 10 keV, and low-temperature measurements were  
139 performed using an ARS close-cycle cryostat. Additional experimental details have been  
140 provided elsewhere<sup>41</sup>. Synchrotron radiation experiments were conducted at the FinEstBeAMS  
141 beamline, MAX IV Laboratory, Sweden, in the energy range of 4.5-11 eV<sup>42,43</sup>. To minimize  
142 higher-order incident light effects,  $\text{MgF}_2$  or fused silica filters were employed depending on  
143 the excitation range. Luminescence was detected using an Andor Shamrock SR-303i  
144 spectrometer coupled with a Hamamatsu H8259-01 photon counting head. The excitation  
145 spectra were normalized to the incident photon flux using a calibrated AXUV100G photodiode.  
146 Luminescence spectra were converted into the energy scale upon using the Jacobian  
147 transformation procedure.

### 148 3. Results and Discussion

#### 149 3.1. Structural and morphological analysis

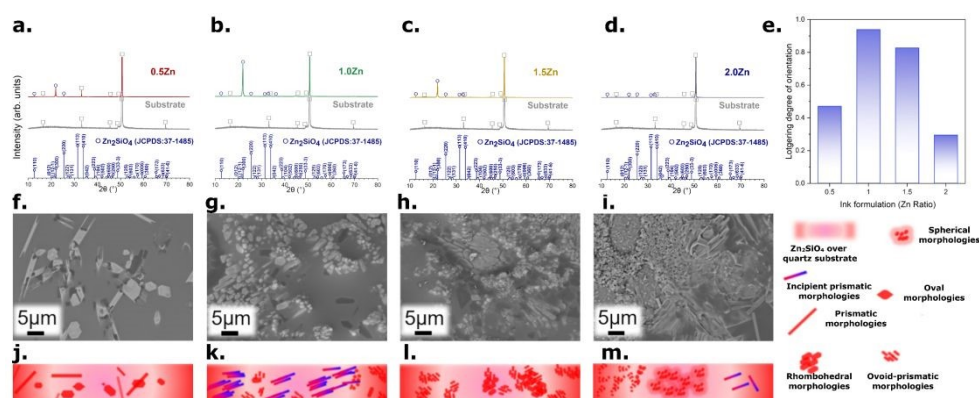
150 The fabrication of  $\text{Zn}_2\text{SiO}_4$  films was studied as a function of ZnO/ $\text{SiO}_2$  ratio (0.5Zn, 1.0Zn,  
151 1.5Zn, and 2.0Zn) and thermal treatment (1100 °C and 1200 °C). This approach was designed  
152 to elucidate the fundamental mechanisms governing phase formation, crystallographic  
153 orientation, and microstructural evolution in the presence of the NaCl-KCl eutectic flux.



### 154 3.1.1. Phase formation and crystallographic texture

View Article Online  
DOI: 10.1039/D6TC00560H

155 XRD analysis (**Fig. 1a-d** and **2a-d**) revealed  $\text{Zn}_2\text{SiO}_4$  as the predominant phase across all  
156 compositions, crystallizing in the rhombohedral structure (space group R-3, JCPDS card No.  
157 37-1485, unit cell parameters:  $a=b=13.938 \text{ \AA}$ ,  $c=9.310 \text{ \AA}$ )<sup>44</sup>. Minor residual ZnO was detected  
158 only in the zinc-rich formulations, evidenced by a low-intensity diffraction peak at  
159 approximately  $36.11^\circ$ , corresponding to the (101) reflection of ZnO. However, the contribution  
160 of this secondary phase was minimal and nearly negligible. No systematic increase in ZnO-  
161 related reflections was observed upon increasing the thermal treatment from  $1100^\circ\text{C}$  to  $1200$   
162  $^\circ\text{C}$ , indicating preservation of the  $\text{Zn}_2\text{SiO}_4$  phase within the investigated temperature range.  
163 This observation is further supported by uniform Zn, Si, and O distributions revealed by EDS  
164 (see **Supplementary Information, Fig. S1**), confirming the overall phase purity of the films  
165 at both processing temperatures. The high phase conversion efficiency, particularly notable at  
166 sub-stoichiometric zinc contents, demonstrates the eutectic salt mixture's effectiveness in  
167 mediating the  $\text{ZnO-SiO}_2$  reaction.



168 **Fig. 1** Structural and morphological characterization of  $\text{Zn}_2\text{SiO}_4$  films synthesized at  $1100^\circ\text{C}$ : (**a-d**) XRD data  
169 for different ZnO concentrations (0.5Zn, 1.0Zn, 1.5Zn, and 2.0Zn), (**e**) calculated Lotgering factors, (**f-i**) SEM  
170 micrographs, and (**j-m**) schematic representations of observed morphologies. The legend indicates the different  
171 morphological features observed across compositions.  
172

173 This conversion efficiency enhancement can be attributed to the two primary mechanisms: (i)  
174 increased atomic mobility in the molten state, and (ii) reduced interfacial energy barriers  
175 between reactant phases, as evidenced by the previous studies on similar systems<sup>45,46</sup>.

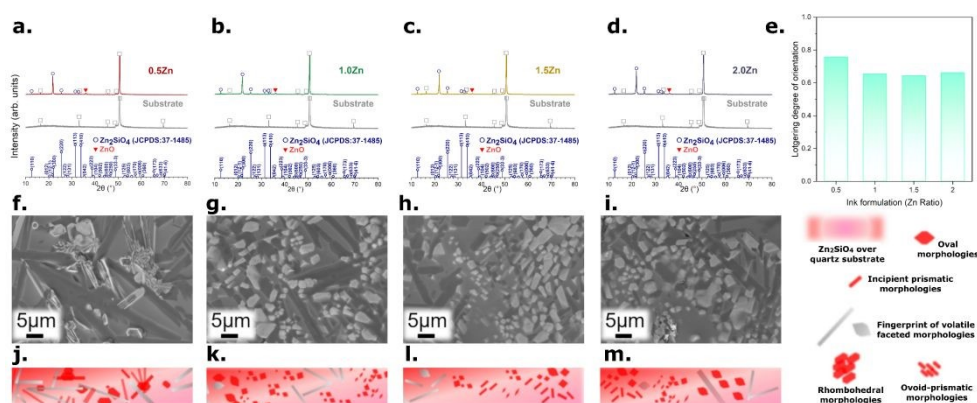
176 The films exhibited strong preferential orientation along the (300) crystallographic plane  
177 ( $2\theta=22.03^\circ$ ), quantified using the Lotgering factor. At  $1100^\circ\text{C}$  (**Fig. 1e**), LF values showed a  
178 distinct composition dependence: 0.47, 0.94, 0.83, and 0.29 for the 0.5Zn, 1.0Zn, 1.5Zn, and  
179 2.0Zn compositions, respectively.



180 The near-unity LF value obtained for the 1.0Zn sample (LF = 0.94) indicates highly textured  
 181 growth and suggests a favourable crystallographic alignment between the  $\text{Zn}_2\text{SiO}_4$  (300) plane  
 182 and the quartz (0001) substrate surface.

183 Quantitative lattice matching analysis (see **Supplementary Information, S2**) indicates a low  
 184 lattice mismatch ( $\sim -0.55\%$ ), suggesting good structural compatibility at the film-substrate  
 185 interface. This structural compatibility, further promoted by the molten salt flux, enhances  
 186 interfacial diffusion and favours oriented  $\text{Zn}_2\text{SiO}_4$  nucleation during film growth.

187 The marked decrease in the Lotgering factor (LF) to 0.29 for the 2.0Zn sample indicates a  
 188 significant disruption in the preferential crystallization process caused by excess ZnO. This  
 189 disruption is likely driven by two concurrent mechanisms: (i) the formation of zinc-rich regions  
 190 that exceed the local solubility limit in the flux, promoting uncontrolled nucleation, and (ii)  
 191 increased competition between heterogeneous nucleation at the substrate interface and  
 192 homogeneous nucleation within the film volume. These competing processes are consistent  
 193 with classical nucleation theory, wherein local supersaturation can dominate over preferred  
 194 orientation mechanisms<sup>47</sup>.



195  
 196 **Fig. 2** Structural and morphological characterization of  $\text{Zn}_2\text{SiO}_4$  films synthesized at 1200 °C: (a-d) XRD data  
 197 for different ZnO concentrations (0.5Zn, 1.0Zn, 1.5Zn, and 2.0Zn), (e) calculated Lotgering factors, (f-i) SEM  
 198 micrographs, and (j-m) schematic representations of observed morphologies. The legend indicates the different  
 199 morphological features observed across compositions.

200 Thermal treatment at 1200 °C reduced this compositional sensitivity (**Fig. 2e**), yielding more  
 201 uniform LF values (0.76, 0.66, 0.64, and 0.66 for 0.5Zn, 1.0Zn, 1.5Zn, and 2.0Zn, respectively).  
 202 This convergence suggests a transition from kinetically controlled growth at 1100 °C to  
 203 thermodynamically dominated processes at higher temperatures, where enhanced atomic  
 204 mobility diminishes the influence of initial compositional variations.



205 To further quantify the microstructural characteristics of the films, the crystallite size was  
206 estimated from the broadening of the (300) diffraction peak. The calculated crystallite sizes for  
207 films synthesized at 1100 °C are approximately 69, 42, 40, and 35 nm for 0.5Zn, 1.0Zn, 1.5Zn,  
208 and 2.0Zn compositions, respectively. For the films processed at 1200 °C, the crystallite sizes  
209 increase to approximately 100, 62, 56, and 41 nm, indicating enhanced crystallite growth driven  
210 by higher atomic mobility at elevated temperature. The decrease in crystallite size with  
211 increasing Zn content at both temperatures suggests a higher nucleation density, which limits  
212 the growth of individual crystallites. This trend is consistent with the composition-dependent  
213 crystallization behaviour discussed above, where increased Zn content promotes competing  
214 nucleation processes. Overall, these results indicate that thermal treatment promotes crystallite  
215 growth, while compositional variations govern nucleation-controlled microstructural  
216 evolution.

### 217 3.1.2. Morphological evolution and growth mechanisms

218 The evolution of film morphology demonstrated a strong correlation with both compositional  
219 variation and crystallographic texture, revealing distinct growth mechanisms at different  
220 processing conditions. The observed morphology of the sample treated at 1100 °C reflects  
221 composition-dependent nucleation and growth behaviour influenced by the molten salt  
222 environment.

223 In the 0.5Zn films (**Fig. 1f, 1j**), the sparse distribution of predominantly rhombohedral particles  
224 aligns with the moderate texturing (LF = 0.47). This morphology suggests growth dominated  
225 by equilibrium crystal faces, where the slow growth rate, limited by zinc availability, allows  
226 the formation of well-defined crystallographic facets. The 1.0Zn composition (**Fig. 1g, 1k**)  
227 showed increased particle density with well-defined prismatic structures, corresponding to the  
228 maximum crystallographic ordering (LF = 0.94). This morphology represents optimal flux-  
229 mediated growth conditions, where the balanced stoichiometry and controlled supersaturation  
230 promote oriented crystal growth through interface-mediated nucleation processes. The 1.5Zn  
231 films (**Fig. 1h, 1l**) exhibited a transition to ovoid-prismatic morphologies with retained  
232 rhombohedral features. The increased particle concentration and morphological diversity  
233 reflect the onset of competing growth mechanisms, consistent with the decreased texture  
234 quality (LF = 0.83). In 2.0Zn films (**Fig. 1i, 1m**), the highest particle density and mixed  
235 morphologies correlate with minimal texturing (LF = 0.29). The emergence of spherical



236 features alongside ovoid-prismatic particles indicates a transition from faceted to rough growth  
237 modes, characteristic of systems exceeding critical supersaturation levels.

238 At 1200 °C, distinct morphological transformations occurred through enhanced diffusion  
239 processes. The characteristic "fingerprint" features observed in 0.5Zn samples (**Fig. 2f, 2j**)  
240 suggest concurrent processes of phase transformation and surface reconstruction through  
241 partial volatilization of the flux components. These surface features likely represent traces of  
242 localized substrate transformation, where quartz undergoes structural modification through  
243 interaction with the molten salt flux. The progressive reduction in these morphological  
244 characteristics with increasing zinc content correlates with enhanced reaction kinetics and  
245 higher particle density, leading to more uniform film surface coverage.

246 These observations highlight the complex interplay between kinetic and thermodynamic  
247 factors governing film morphology. At 1100 °C, film growth is primarily governed by  
248 composition-dependent kinetics, giving rise to distinct morphological regimes that are highly  
249 sensitive to local supersaturation and nucleation dynamics. In contrast, at 1200 °C, enhanced  
250 atomic mobility and surface diffusion promote more uniform morphological characteristics,  
251 largely independent on initial composition. This understanding underscores the potential for  
252 precise control of film microstructure through deliberate tuning of processing temperature and  
253 compositional parameters, offering a robust framework for tailoring texture and morphology  
254 in flux-assisted film synthesis.

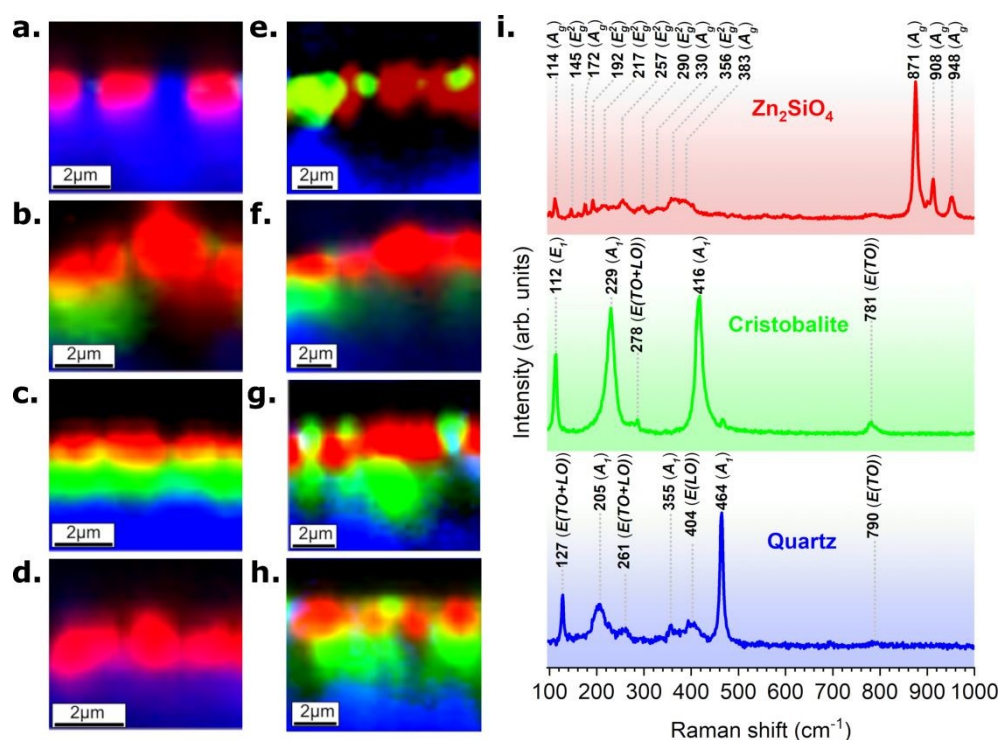
255 The correlation between structural and morphological characteristics demonstrates the critical  
256 role of the molten salt flux in mediating both atomic transport and crystal growth processes.  
257 While XRD and SEM analyses have provided comprehensive insights into crystallographic  
258 ordering and surface features, a complete understanding of the film formation mechanism  
259 requires investigation of interfacial phenomena. The following section examines these aspects  
260 through depth-resolved Raman spectroscopy, which reveals the role of the molten salt flux in  
261 mediating substrate transformation and phase formation at the film-substrate interface.

### 262 **3.1.3. Interface evolution and phase transformation analysis**

263 Depth-resolved Raman spectroscopy provided critical insights into interfacial phenomena and  
264 phase evolution, complementing the structural and morphological characterization. The depth-  
265 profile images (**Fig. 3a-h**) illustrate the distribution of phases across the film-substrate



266 interface, where the colour contrast distinguishes between  $\text{Zn}_2\text{SiO}_4$  (red), cristobalite (green),  
 267 and quartz substrate (blue).



268  
 269 **Fig. 3** Interface analysis of  $\text{Zn}_2\text{SiO}_4$  films: **(a-d)** Raman depth profile images of films with different ZnO  
 270 concentrations (0.5Zn, 1.0Zn, 1.5Zn, and 2.0Zn) synthesized at 1100 °C, **(e-h)** corresponding profiles at 1200  
 271 °C, and **(i)** representative Raman spectra showing characteristic vibrational modes of quartz, cristobalite, and  
 272  $\text{Zn}_2\text{SiO}_4$  phases. Color contrast indicates quartz (blue), cristobalite (green), and  $\text{Zn}_2\text{SiO}_4$  (red).

273 At 1100 °C, the interface evolution demonstrates complex interplay between salt-mediated  
 274 phase transformation with the assistance of molten salt and direct  $\text{Zn}_2\text{SiO}_4$  formation. In the  
 275 0.5Zn films (**Fig. 3a**), the analysis reveals non-continuous  $\text{Zn}_2\text{SiO}_4$  formation at the interface,  
 276 characterized by distinct regions of  $\text{Zn}_2\text{SiO}_4$  alternated with exposed quartz substrate. This  
 277 discontinuous interface structure results from limited zinc availability and insufficient  
 278 concentration of  $\text{Na}^+$  and  $\text{K}^+$  ions from the eutectic salt mixture. These alkali metal ions, when  
 279 present in adequate concentrations, can weaken Si-O bonds in the quartz structure through ionic  
 280 interactions, facilitating the reorganization of the  $\text{SiO}_4$  tetrahedra necessary for cristobalite  
 281 formation<sup>48</sup>. The emergence of cristobalite in the 1.0Zn films (**Fig. 3b**) and its development  
 282 into a continuous interlayer in the 1.5Zn samples (**Fig. 3c**) reflects the increasing effectiveness  
 283 of the molten salt assisted transformation as more  $\text{Na}^+$  and  $\text{K}^+$  cations become available. This  
 284 progression indicates that the eutectic salt mixture not only serves as a reaction medium but  
 285 actively participates in the substrate transformation through cationic interactions with the



286 quartz surface. The absence of cristobalite in the 2.0Zn films (**Fig. 3d**) reveals a competing  
 287 mechanism where high zinc content creates sufficient chemical potential gradient to bypass the  
 288 intermediate cristobalite formation. The direct formation of  $\text{Zn}_2\text{SiO}_4$  is facilitated by enhanced  
 289 ZnO dissolution in the molten flux, which promotes immediate reaction with the quartz  
 290 substrate rather than enabling its phase transformation. This accelerated interface reaction  
 291 correlates with the significantly reduced crystallographic texturing (Lotgering factor,  $\text{LF} =$   
 292  $0.29$ ) observed in XRD analysis, indicating that rapid, uncontrolled nucleation at the interface  
 293 disrupts the development of long-range orientational order. At  $1200\text{ }^\circ\text{C}$  (**Fig. 3e-h**), the  
 294 consistent formation of cristobalite across all compositions indicates an enhancement in alkali  
 295 ion diffusion and accelerated quartz transformation. This temperature-dependent behaviour  
 296 appears largely independent of zinc content, suggesting that the dominant mechanism is  
 297 thermally activated ionic mobility within the molten salt environment<sup>48</sup>. Supporting evidence  
 298 from SEM analysis reveals characteristic surface features associated with high-temperature  
 299 phase transitions, further corroborating the occurrence of quartz-to-cristobalite transformation.  
 300 The interface structure results from competing kinetics between cristobalite formation and  
 301  $\text{Zn}_2\text{SiO}_4$  growth, both assisted by the molten salt flux. The depth-resolved Raman analysis  
 302 enabled precise measurement of film thicknesses across compositions and processing  
 303 conditions. At  $1100\text{ }^\circ\text{C}$ , the thickness measurements ( $1.41\text{ }\mu\text{m}$  for 0.5Zn,  $1.60\text{ }\mu\text{m}$  for 1.0Zn,  
 304  $1.04\text{ }\mu\text{m}$  for 1.5Zn, and  $1.40\text{ }\mu\text{m}$  for 2.0Zn) show maximum value at 1.0Zn, correlating with  
 305 optimal crystallographic texturing ( $\text{LF} = 0.94$ ) and initial cristobalite formation. These  
 306 thickness measurements were further confirmed by cross-sectional SEM micrographs (see  
 307 **Supplementary Information, Fig. S3**). This correlation suggests that controlled interface  
 308 transformation promotes uniform film growth through regulated mass transport. At  $1200\text{ }^\circ\text{C}$ ,  
 309 increased thicknesses ( $2.21$ ,  $1.71$ ,  $1.47$ , and  $1.50\text{ }\mu\text{m}$  for 0.5Zn, 1.0Zn, 1.5Zn, and 2.0Zn,  
 310 respectively) reflect enhanced diffusion processes, consistent with the more uniform  
 311 morphological characteristics and LF values observed at higher temperatures.

312 The Raman spectra (**Fig. 3i**) provide detailed vibrational characteristics of the three distinct  
 313 phases present in the system. The complete list of Raman modes and their assignments for all  
 314 observed phases are presented in **Table 1**.

**Table 1. Raman active modes and symmetry assignments of identified phases**

SiO <sub>2</sub> (Quartz)		SiO <sub>2</sub> (Cristobalite)		Zn <sub>2</sub> SiO <sub>4</sub>	
Wavenumber (cm <sup>-1</sup> )	Assignment <sup>49</sup>	Wavenumber (cm <sup>-1</sup> )	Assignment <sup>50</sup>	Wavenumber (cm <sup>-1</sup> )	Assignment <sup>51</sup>



127	$E(TO + LO)$	112	$E_1$	114	$A_g$
205	$A_1$	229	$A_1$	145	$E_g^2$
261	$E(TO + LO)$	278	$E(TO + LO)$	172	$A_g$
355	$A_1$	416	$A_1$	192	$E_g^2$
404	$E(LO)$	781	$E(TO)$	217	$E_g^2$
464	$A_1$	-	-	257	$E_g^2$
790	$E(TO)$	-	-	290	$E_g^2$
-	-	-	-	330	$A_g$
-	-	-	-	356	$E_g^2$
-	-	-	-	383	$A_g$
-	-	-	-	871	$A_g$
-	-	-	-	908	$A_g$
-	-	-	-	948	$A_g$

View Article Online  
DOI: 10.1039/D6TC00560H

315 The quartz substrate exhibits characteristic modes at 127, 205, 261, 355, 404, 464, and 790 cm<sup>-1</sup>,  
 316 corresponding to the  $E(TO + LO)$ ,  $A_1$ ,  $E(TO + LO)$ ,  $A_1$ ,  $E(LO)$ ,  $A_1$ , and  $E(TO)$  symmetries,  
 317 respectively<sup>40</sup>. The formation of cristobalite is confirmed by the distinctive peaks at 112 ( $E_1$ ),  
 318 229 ( $A_1$ ), 278 ( $E(TO + LO)$ ), 416 ( $A_1$ ), and 781 cm<sup>-1</sup> ( $E(TO)$ )<sup>50</sup>, reflecting the modified  
 319 tetrahedral arrangement in the transformed phase. The  $Zn_2SiO_4$  phase exhibits multiple  
 320 vibrational modes between 114 and 948 cm<sup>-1</sup>, with particularly intense bands at 871 cm<sup>-1</sup>  
 321 (symmetric Si-O stretching) and 908, 948 cm<sup>-1</sup> (asymmetric stretching)<sup>52</sup>.

322 The correlation between the interface structure and processing parameters reveals that the film  
 323 formation mechanism is governed by the interplay between salt-mediated phase transformation  
 324 and direct  $Zn_2SiO_4$  crystallization controlled by alkali ion concentration, ZnO content, and  
 325 processing temperature. Understanding these relationships enables precise control over  
 326 interface structure and film thickness, demonstrating the effectiveness of the molten salt-  
 327 assisted screen printing strategy for tunable thin film fabrication. The achievement of highly  
 328 textured  $Zn_2SiO_4$  films with well-defined interfaces and controlled thickness represents a  
 329 crucial step in materials development for deep UV emission. The following section examines  
 330 how these structural characteristics influence the deep UV luminescence properties,  
 331 particularly focusing on the relationship between interface quality, crystallographic ordering,  
 332 and emission in the deep UV spectral range.



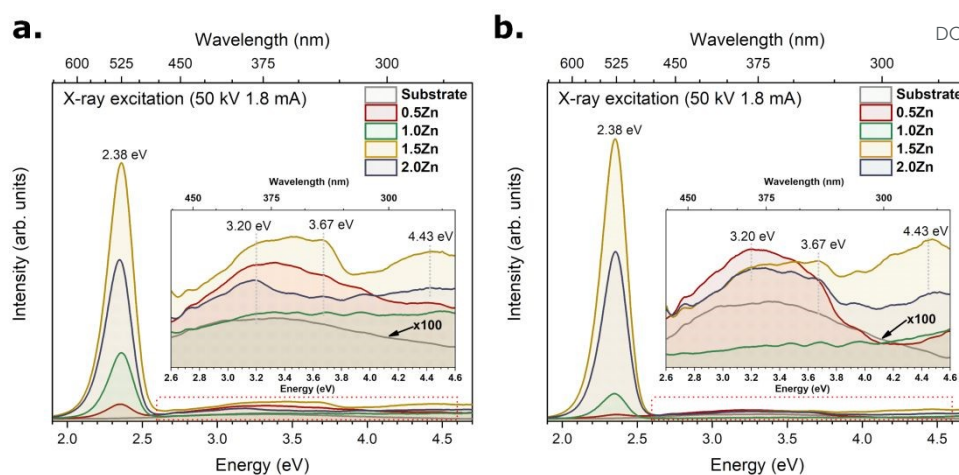
## 333 3.2. Luminescence characterization

334 The luminescent properties of  $\text{Zn}_2\text{SiO}_4$  films were investigated through three complementary  
335 spectroscopic techniques. X-ray excited optical luminescence at room temperature (RT)  
336 provided initial insights into the overall emission characteristics, while temperature-dependent  
337 cathodoluminescence measurements at RT and 6 K enabled detailed examination of the deep  
338 UV emission features. Further understanding of the excitation and emission processes was  
339 achieved through synchrotron radiation-excited photoluminescence at 6 K, which allowed  
340 selective excitation across a wide energy range and precise monitoring of the deep UV  
341 response.

### 342 3.2.1. X-ray luminescence

343 XEOL spectroscopy, effective for probing both surface and bulk luminescent properties<sup>53</sup>, has  
344 demonstrated significant utility in investigating silicate-based nanoscintillators<sup>54</sup>. Due to X-ray  
345 penetration depths significantly exceeding the film thicknesses (1.04-2.21  $\mu\text{m}$ ), the  
346 measurements probe contributions from both the films and the substrate. **Fig. 4** presents RT  
347 XEOL spectra of all film compositions at both processing temperatures alongside the quartz  
348 substrate for comparison. The measurements reveal multiple emission features that reflect the  
349 complex interplay between composition, interface structure, and phase transformation  
350 processes established through our structural analyses. The dominant emission band centred at  
351 2.38 eV (521 nm), characteristic of  $\text{Mn}^{2+}$  transitions in tetrahedral coordination<sup>55</sup>, exhibits  
352 maximum intensity in 1.5Zn samples at both processing temperatures. This band is absent in  
353 the substrate spectrum, confirming its origin from the film. The dominance of  $\text{Mn}^{2+}$  emission  
354 despite trace impurity levels indicates efficient energy transfer to these luminescent centres,  
355 enhancing the multifunctionality of the films in accordance with previous studies of silicate-  
356 based materials<sup>56</sup>. The high-energy region of the spectra, highlighted in the insets of **Fig. 4a-**  
357 **b**, provides insights into the relationship between structural evolution and luminescent  
358 properties. The band at 3.20 eV (387 nm), attributed to near-band-edge transitions in  $\text{ZnO}$ <sup>57</sup>,  
359 reflects residual  $\text{ZnO}$  identified in XRD analysis. The feature at 3.67 eV (338 nm),  
360 corresponding to non-bridging oxygen hole centres in silica<sup>58</sup>, appears in both film and  
361 substrate spectra, indicating contributions from the quartz substrate and  $\text{SiO}_2$  polymorphs  
362 within the films.



View Article Online  
DOI: 10.1039/D6TC00560H

363

364 **Fig. 4** X-ray excited luminescence analysis of  $\text{Zn}_2\text{SiO}_4$  film-substrate systems: room temperature XEOL spectra  
 365 of samples heat-treated at (a) 1100 °C and (b) 1200 °C with different ZnO concentrations (0.5Zn, 1.0Zn,  
 366 and 2.0Zn). The quartz substrate spectrum is multiplied by 100 for better visualization. The insets highlight the  
 367 high-energy region showing weak emission features in the UV range.

368 A weak deep UV emission at 4.43 eV (280 nm), absent in the substrate, is also detected,  
 369 showing the highest intensity in 1.5Zn samples at both synthesis temperatures. This  
 370 composition-dependent behaviour is consistent with the interface development observed in  
 371 1.5Zn films, where the formation of a continuous cristobalite interlayer could potentially  
 372 influence the emission properties.

373 To further investigate the nature of these emission features, particularly the deep UV response,  
 374 temperature-dependent cathodoluminescence measurements were performed on the 1.5Zn  
 375 films synthesized at both temperatures, which exhibited the most pronounced XEOL emission  
 376 bands.

### 377 3.2.2. Cathodoluminescence

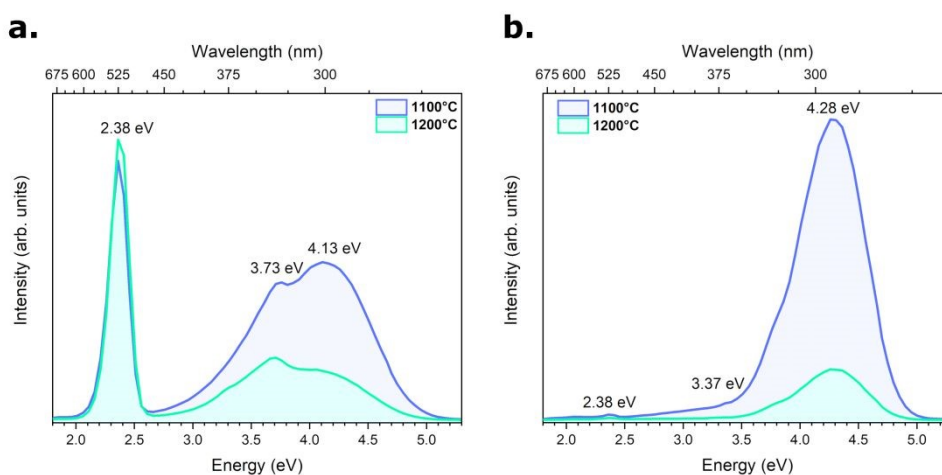
378 The cathodoluminescence spectra presented in **Fig. 5** reveal significant temperature dependent  
 379 emission characteristics in 1.5Zn films at RT vs 6 K. RT spectra shown in **Fig. 5a** display the  
 380 characteristic  $\text{Mn}^{2+}$  emission at 2.38 eV (521 nm) alongside a broad UV band with features at  
 381 3.73 eV (332 nm) and 4.13 eV (300 nm). Films synthesized at 1100 °C, characterized by higher  
 382 crystallographic ordering (LF = 0.83), exhibit enhanced UV emission compared to those  
 383 processed at 1200 °C (LF = 0.64).

384 The emission spectrum of the material recorded at low temperatures (6 K) is remarkably  
 385 different from that measured at RT, as illustrated in **Fig. 5b**.



386 The deep UV emission shifts to higher energy (4.28 eV (290 nm)) and becomes dominant  
 387 while the Mn<sup>2+</sup>-related green emission is substantially suppressed. The film synthesized at 1100  
 388 °C shows markedly enhanced UV emission intensity relative to the sample synthesized at 1200  
 389 °C, which correlates with its improved crystallographic texturing and more homogeneous  
 390 interface structure associated with the presence of a cristobalite interlayer.

391 The cristobalite interlayer is likely to provide a more structurally uniform transition region at  
 392 the film-substrate interface, which may reduce the density of interfacial defects acting as non-  
 393 radiative recombination centres. As a result, excitonic recombination within the Zn<sub>2</sub>SiO<sub>4</sub> lattice  
 394 is less hindered, contributing to the enhanced deep UV emission. In contrast, the more complex  
 395 interface structure and increased lattice disorder in the 1200 °C sample are expected to  
 396 introduce additional non-radiative recombination pathways for charge carriers, which compete  
 397 with the radiative UV transitions.



398  
 399 **Fig. 5** Cathodoluminescence spectra of Zn<sub>2</sub>SiO<sub>4</sub> films with 1.5Zn concentration synthesized at 1100 °C and  
 400 1200 °C, recorded at (a) room temperature and (b) 6 K.

401 The dependence of the CL spectrum on film quality suggests that the observed deep UV  
 402 emission is predominantly intrinsic, arising from electronic transitions within the Zn<sub>2</sub>SiO<sub>4</sub>  
 403 crystal structure rather than from defect-related centres.

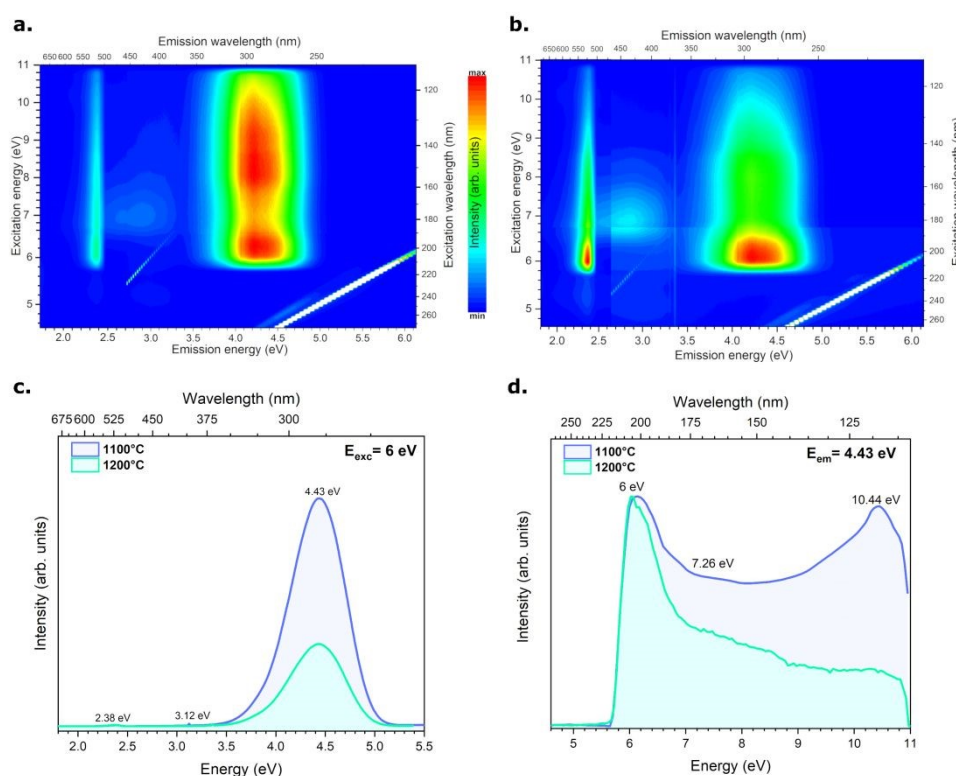
404 To further elucidate the nature of these transitions, synchrotron radiation based selective  
 405 spectroscopy was employed, providing valuable information on the excitation mechanisms and  
 406 the origin of electronic states responsible for the deep UV emission in Zn<sub>2</sub>SiO<sub>4</sub>.

### 407 3.2.3. Photoluminescence under synchrotron radiation excitation



408 To further investigate the mechanism responsible for the deep UV emission, synchrotron  
 409 radiation studies were conducted at 6 K (Fig. 6).

410 As shown in Fig. 6a-b, the 2D excitation-emission maps reveal the luminescence response  
 411 across a wide range of excitation energies. While samples synthesized at both temperatures  
 412 exhibit similar spectral features, the sample synthesized at 1100 °C demonstrates notably  
 413 higher emission intensity. The emission spectra presented in Fig. 6c, measured under 6 eV (207  
 414 nm) excitation, display a dominant peak at 4.43 eV (280 nm). This deep UV emission shows  
 415 enhanced intensity in the sample synthesized at 1100 °C, corroborating the pattern observed in  
 416 low-temperature CL measurements. At 6 K, both Mn<sup>2+</sup> emission at 2.38 eV (521 nm) and the  
 417 feature at 3.12 eV (397 nm) are significantly reduced.



418  
 419 **Fig. 6** Synchrotron excitation analysis of Zn<sub>2</sub>SiO<sub>4</sub> films with 1.5Zn concentration: (a, b) 2D excitation-emission  
 420 maps of films synthesized at 1100 °C (a) and 1200 °C (b), (c) emission spectra under 6 eV excitation, and (d)  
 421 excitation spectra monitored at 4.43 eV emission. All measurements were performed at 6 K.

422 **Fig. 6d** shows the excitation spectra monitored at 4.43 eV (280 nm), providing crucial insights  
 423 into the origin of this deep UV emission. A recent study of sol-gel synthesized Zn<sub>2</sub>SiO<sub>4</sub>  
 424 powders demonstrated that this emission originates from host excitons, either self-trapped or  
 425 perturbed by lattice defects such as oxygen vacancies<sup>28</sup>. The excitation spectra support and  
 426 expand this understanding, showing an onset at 6.0 eV (207 nm), corresponding to the



427 fundamental band gap of zinc silicate derived from partial density of states (PDOS)  
428 calculations<sup>59</sup> and consistent with the band gap values previously estimated from diffuse  
429 reflectance spectra of Zn<sub>2</sub>SiO<sub>4</sub> powders synthesized at 1000, 1100, 1200, and 1300 °C<sup>28</sup> (see  
430 **Supplementary Information, Fig. S4**). This excitation feature is therefore associated with  
431 band-to-band transitions leading to the formation of host excitons. In contrast, at higher  
432 excitation energies (above ~7 eV), the excitation processes increasingly involve transitions  
433 within the [SiO<sub>4</sub>]<sup>4-</sup> units and defect-related states, as reported in previous studies<sup>60</sup>.

434 The high-energy region of the excitation spectra is thus related to the fundamental absorption  
435 processes characterized by the creation of mobile electrons in the conduction band and holes  
436 in the valence band due to the transitions from 2p O to 4s Zn and 3s Si states. These states have  
437 been shown to be well dispersive in Zn<sub>2</sub>SiO<sub>4</sub> (see, *e.g.*,<sup>27</sup>), enabling high mobility of electrons  
438 in the conduction band, which in turn can lead to high energy losses of electrons with high  
439 kinetic energy at the crystal surface and defects<sup>61</sup>. This renders luminescence highly sensitive  
440 to material structural quality and defect distribution. Indeed, in the sample synthesized at 1100  
441 °C, this high-energy region of the excitation spectrum is remarkably intense, indicating  
442 differences in the excitation processes and carrier relaxation dynamics between the two  
443 samples.

444 The influence of lattice defects can be considered in terms of intrinsic point defects and  
445 structural disorder. In related oxide systems such as ZnAl<sub>2</sub>O<sub>4</sub>, deep UV emission has been  
446 linked to excitons perturbed by oxygen vacancies, as confirmed by electron paramagnetic  
447 resonance (EPR) studies<sup>21</sup>. Similar defect-exciton interactions may also be expected in  
448 Zn<sub>2</sub>SiO<sub>4</sub>, where lattice imperfections can influence exciton localization and recombination.  
449 However, the specific nature and concentration of defects in the present films cannot be  
450 determined within the scope of this study. Further investigations, such as time-resolved  
451 photoluminescence and EPR measurements, will be pursued to clarify the role of defects in the  
452 luminescence response of Zn<sub>2</sub>SiO<sub>4</sub>.

453 The stronger deep UV emission in the sample synthesized at 1100 °C is consistent with its  
454 well-defined cristobalite interlayer and high crystallographic texturing (LF = 0.83), which may  
455 contribute to reduced non-radiative recombination. Importantly, the lower emission intensity  
456 observed in the 1200 °C sample is unlikely to originate from thermal decomposition of  
457 Zn<sub>2</sub>SiO<sub>4</sub>. The ZnO-SiO<sub>2</sub> phase diagram indicates that Zn<sub>2</sub>SiO<sub>4</sub> remains thermodynamically  
458 stable up to approximately 1400 °C<sup>62,63</sup>, and our previous quantitative phase analysis of



459 powders synthesized up to 1300 °C confirmed phase stability under comparable conditions.  
460 Thermogravimetric and differential scanning calorimetry (TGA–DTG–DSC) of Zn<sub>2</sub>SiO<sub>4</sub>  
461 powders synthesized at 1300 °C via the molten salt route demonstrate that fully crystallized  
462 Zn<sub>2</sub>SiO<sub>4</sub> remains thermally stable upon reheating within the investigated temperature range  
463 (see **Supplementary Information, Fig. S5**). Therefore, the observed luminescence differences  
464 are attributed to microstructural and interfacial variations rather than changes in phase  
465 composition.

#### 466 4. Conclusions

467 Zn<sub>2</sub>SiO<sub>4</sub> has been identified as a promising rare-earth-free deep UV emitter. However, the  
468 extension of its intrinsic emission properties to film form remains limited. The successful  
469 fabrication of highly textured Zn<sub>2</sub>SiO<sub>4</sub> films featuring well-defined interfaces and controlled  
470 thickness in this work demonstrates the feasibility of intrinsic deep UV emission in film form.  
471 The optimal structural and luminescent properties were achieved in samples synthesized at  
472 1100 °C with a 1.5Zn composition, where the formation of a continuous cristobalite interlayer  
473 and a high Lotgering factor (LF = 0.83) enabled superior crystallographic texturing.

474 This study addresses the relationship between processing-induced structural evolution,  
475 interface formation, and intrinsic deep UV emission in Zn<sub>2</sub>SiO<sub>4</sub> films.

476 By systematically correlating processing conditions with structural evolution and optical  
477 response, this work clarifies how interfacial phase transformation and crystallographic  
478 orientation influence intrinsic deep UV emission in Zn<sub>2</sub>SiO<sub>4</sub> films.

479 The molten salt flux plays a multifaceted role by mediating phase formation, controlling  
480 interface evolution, and promoting oriented growth, although excessive ZnO disrupts texture  
481 development. Spectroscopic and synchrotron-based studies indicate that the deep UV emission  
482 at 4.43 eV (280 nm) arises from intrinsic electronic transitions involving self-trapped or defect-  
483 perturbed excitons in Zn<sub>2</sub>SiO<sub>4</sub>. The strong correlation between structural order and emission  
484 intensity highlights the critical impact of controlled processing on optical performance.

485 The screen printing method assisted by a molten salt eutectic flux provides a simple, scalable,  
486 and effective route for synthesizing phase-pure, highly oriented Zn<sub>2</sub>SiO<sub>4</sub> films without complex  
487 vacuum processing.

488 Overall, this work addresses the limited understanding of intrinsic deep UV emission in  
489 Zn<sub>2</sub>SiO<sub>4</sub> films and demonstrates the potential of rare-earth- and heavy-metal-free Zn<sub>2</sub>SiO<sub>4</sub>



490 materials for next-generation deep-UV radiation sources, while the structural control achieved  
491 here illustrates the broader potential of this processing approach for oxide-based photonic  
492 materials.

[View Article Online](#)  
DOI: 10.1039/D6TC00560H

493

494

495

496

497

498

499

500

501

502

503

504

505

506

507

508

509

510

511

512

513

514



515 **Corresponding Author**View Article Online  
DOI: 10.1039/D6TC00560H516 \*E-mail: [Jallouli.necib@taltech.ee](mailto:Jallouli.necib@taltech.ee)517 ORCID 518 Jallouli Necib: [0000-0003-1425-6835](https://orcid.org/0000-0003-1425-6835)

519

520 ORCIDs  of co-authors521 Eduard Feldbach: [0000-0003-1536-7211](https://orcid.org/0000-0003-1536-7211)522 Ivo Romet: [0009-0006-7146-4277](https://orcid.org/0009-0006-7146-4277)523 Vitaly Nagirnyi: [0000-0001-6833-6406](https://orcid.org/0000-0001-6833-6406)524 Irina Hussainova: [0000-0003-3081-2491](https://orcid.org/0000-0003-3081-2491)525 Thomas Jüstel: [0000-0002-9455-5044](https://orcid.org/0000-0002-9455-5044)526 Rocío R. Rojas-Hernandez: [0000-0001-7808-218X](https://orcid.org/0000-0001-7808-218X)

527

528 **CRedit authorship contribution statement**

529 **Jallouli Necib:** Writing – review & editing, Writing – original draft, Validation, Methodology, Investigation,  
 530 Formal analysis, Conceptualization. **Eduard Feldbach:** Writing – review & editing, Formal analysis. **Ivo**  
 531 **Romet:** Writing – review & editing, Investigation. **Vitaly Nagirnyi:** Writing – review & editing, Writing –  
 532 original draft, Validation, Methodology, Investigation. **Irina Hussainova:** Writing – review & editing,  
 533 Validation, Investigation. **Thomas Jüstel:** Writing – review & editing, Investigation. **Rocío E. Rojas-**  
 534 **Hernandez:** Writing – review & editing, Writing – original draft, Visualization, Validation, Supervision,  
 535 Software, Resources, Project administration, Methodology, Investigation, Funding acquisition, Formal analysis,  
 536 Data curation, Conceptualization.

537

538 **Conflict of Interest**

539 The authors declare no conflict of interest.

540 **Data Availability**

541 Data for this article, including raw XRD patterns, SEM images, cathodoluminescence spectra, and X-ray excited  
 542 optical luminescence spectra, are available at the TalTech Data Repository at [https://doi.org/10.48726/qgpyy-](https://doi.org/10.48726/qgpyy-k5q16)  
 543 [k5q16](https://doi.org/10.48726/qgpyy-k5q16). Supplementary information (SI) containing additional cross-sectional SEM micrographs demonstrating  
 544 film thickness and interface morphology across different processing temperatures and compositions.

545 **Acknowledgments**

546 The financial support from the Estonian Research Council (grants PSG-466 (R. E. Rojas-Hernandez), PRG-  
 547 643&PRG3028 (I. Hussainova), PRG2733 (V. Nagirnyi)) is gratefully acknowledged. Researchers from the  
 548 University of Tartu, Estonia were supported also by the ERDF funding's in Estonia granted to the Centre of  
 549 Excellence TK141 "Advanced materials and high-technology devices for sustainable energetics, sensorics and  
 550 nanoelectronics (HiTechDevices)" (grant no. TK141 2014–2020.4.01.15-0011). R.E.R.H acknowledges the  
 551 financial support from project PID2023- 153398OB-I00 funded by MCIU/AEI/10.13039/501100011033 and the  
 552 European Social Fund Plus (ESF+). We acknowledge MAX IV Laboratory for time on Beamline FinEstBeAMS  
 553 under Proposal 20230209. Research conducted at MAX IV, a Swedish national user facility, is supported by the  
 554 Swedish Research council under contract 2018-07152, the Swedish Governmental Agency for Innovation Systems  
 555 under contract 2018-04969, and Formas under contract 2019-02496.



556 **References**

- 557 1. A. Gidari, S. Sabbatini, S. Bastianelli, S. Pierucci, C. Busti, D. Bartolini, A. M. Stabile, C.  
558 Monari, F. Galli, M. Rende, G. Cruciani and D. Francisci, *Viruses*, 2021, 13, 408.
- 559 2. M. Kösea, Ç. K. Akkanb, H. Karabacakc and A. Kolumand, *J. Biomed. Res. Environ. Sci.*,  
560 2024, 5, 1358-1370.
- 561 3. S. Wang, Z. Wu, L. Sun, J. Ren, X. Zheng, J. Zhang and J. Ren, *J. Mater. Chem. C*, 2025,13,  
562 6302-6308.
- 563 4. T. Tanaka, N. Sasaki, A. Krisnanda, M. Shinohara, H. Z. Amin, S. Horibe, K. Ito, M. Iwaya,  
564 A. Fukunaga, K. I. Hirata and Y. Rikitake, *J. Am. Heart Assoc.*, 2024, 13, e031639.
- 565 5. S.B. Maji, A. Vanetsev, V. Nagirnyi, K. Chernenko, E. Feldbach, J. Kozlova, H. Mändar, I.  
566 Romet, M. Rähn and M. Kirm, *J. Mater. Chem. C*, 2025,13, 10139-10151.
- 567 6. W. Liu, Y. Wang, H. Qiu, D. Chen, S. Wu, Q. Ji, B. Chang, Y. Li, H. Zhao, Y. Tan and Y. Gu,  
568 *Biomed. Opt. Express*, 2024, 15, 4081-4100.
- 569 7. L. L. Barnkob, A. Argyraki, P. M. Petersen and J. Jakobsen, *Food Chem.*, 2016, 212, 386-391.
- 570 8. R. Escobar-Bravo, P. G. Klinkhamer and K. A. Leiss, *Front. Plant Sci.*, 2017, 8, 278.
- 571 9. R. Hidalgo-Sanz, M. Á. Del-Castillo-Alonso, S. Sanz, C. Olarte, J. Martínez-Abaiagar and E.  
572 Núñez-Olivera, *Agriculture*, 2024, 14, 681.
- 573 10. United Nations Environment Programme (UNEP), Minamata convention on mercury, United  
574 Nations Environment Programme, Nairobi, Kenya, 2013.
- 575 11. P. C. Ricci, *Crystals*, 2020, 10, 559.
- 576 12. H. Diao, H. Yang, T. Tan, G. Ren, M. You, L. Wu, M. Yang, Y. Bai, S. Xia, S. Song and M.  
577 Quintana, *Miner. Eng.*, 2024, 216, 108889.
- 578 13. S. Liu, T. Lu, Y. Yuan, J. Cao, W. Wan, T. Li, T. Wang, Z. Chen, X. Sun and X. Wang, *Adv.*  
579 *Funct. Mater.*, 2025, 35, 2503580.
- 580 14. F. Feng, Y. Liu, K. Zhang, H. Yang, B. R. Hyun, K. Xu, H.S. Kwok and Z. Liu, *Nat. Photonics*,  
581 2025, 19, 101-108.
- 582 15. Z. Lv, Z. Liao, X. Liu, J. Jiang, H. Geng, S. Qi, S. Liu and S. Zhou, *Laser Photonics Rev.*, 2026,  
583 e01763.
- 584 16. D.X. Zhu, G. Wang and Y. F. Li, *Front. Phys.*, 2025, 13, 1718751.
- 585 17. X. Xu, H. P. Liang, Q. S. Huang, Z. Liu, B. Q. Zhao, S. Y. Xu, C. N. Li, Z. K. Zhou, J. Li, S.  
586 H. Wei and X. Zhang, *J. Am. Chem. Soc.*, 2024, 146, 12864-12876.
- 587 18. R.K. Guntu, S.S. Devi, P. Ashok, G. Bhikshamaiah, N.R.K. Chand, S. Sripadha, P.S. Prasad,  
588 C.S. Rao, *J. Mol. Liq.*, 2024, 404, 124933.
- 589 19. R.K. Guntu, *J. Mol. Struct.*, 2022, 1248, 131533.
- 590 20. R. E. Rojas-Hernandez, F. Rubio-Marcos, I. Romet, A. Del Campo, G. Gorni, I. Hussainova, J.  
591 F. Fernandez and V. Nagirnyi, *Inorg. Chem.*, 2022, 61, 11886-11896.
- 592 21. R. E. Rojas-Hernandez, F. Rubio-Marcos, I. Romet, E. Feldbach, M. Buryi, D. John, R. Ivanov,  
593 I. Hussainova, J. F. Fernandez and V. Nagirnyi, *Appl. Mater. Today*, 2024, 38, 102230.
- 594 22. S. Karmakar, I. H. Emu, M. A. Halim, P. K. Sarkar, M. Sultana, A. Tasnim, M. A. Hamid, I. F.  
595 Shiam, R. Droopad and A. Haque, *J. Appl. Phys.*, 2024, 135, 042603.
- 596 23. R. Gerdes, D. Enseling, M. Haase and T. Jüstel, *J. Lumin.*, 2018, 198, 410-417.
- 597 24. P. V. Ramakrishna, D. B. R. K. Murthy, D. L. Sastry and K. Samatha, *Spectrochim. Acta A*,  
598 2014, 129, 274-279.
- 599 25. S. Tripathi, R. Bose, A. Roy, S. Nair and N. Ravishankar, *ACS Appl. Mater. Interfaces*, 2015,  
600 7, 26430-26436.
- 601 26. G. Essalah, G. Kadim, A. Jabar, R. Masrouf, M. Ellouze, H. Guermazi and S. Guermazi, *Ceram.*  
602 *Int.*, 2020, 46, 12656-12664.
- 603 27. S. Zh. Karazhanov, P. Ravindran, H. Fjellvåg and B. G. Svensson, *J. Appl. Phys.*, 2009, 106,  
604 123701.



- 605 28. J. Necib, E. Feldbach, I. Romet, V. Nagirnyi, I. Hussainova and R. E. Rojas-Hernandez, *Lumin.*, 2025, 277, 121070. View Article Online  
DOI: 10.1039/D6TC00560H
- 606
- 607 29. J. Necib, E. Feldbach, I. Romet, V. Nagirnyi, I. Hussainova, T. Jüstel and R. E. Rojas-
- 608 Hernandez, *Ceram. Int.*, 2025, 51, 34922-34931.
- 609 30. X. Feng, X. Yuan, T. Sekiguchi, W. Lin and J. Kang, *J. Phys. Chem. B*, 2005, 109, 15786-
- 610 15790.
- 611 31. Li, Y. Bando, B. Dierre, T. Sekiguchi, Y. Huang, J. Lin and D. Golberg, *Nanoscale Res. Lett.*,
- 612 2010, 5, 773-780.
- 613 32. Dierre, X. Yuan and T. Sekiguchi, *Sci. Technol. Adv. Mater.*, 2010, 11, 043001.
- 614 33. T. Furukawa, S. Kanamori, M. Fukuta, Y. Nawa, H. Kominami, Y. Nakanishi, A. Sugita, W.
- 615 Inami and Y. Kawata, *Opt. Express*, 2015, 23, 18630-18637.
- 616 34. K. C. Peng, H. C. Kao, S. J. Liu, K. L. Tsai and J. C. Lin, *Jpn. J. Appl. Phys.*, 2013, 52, 11NB04.
- 617 35. H. P. Kuo, H. A. Tsai, A. N. Huang and W. C. Pan, *Appl. Energy*, 2016, 164, 1003-1011.
- 618 36. W. Yao, Q. Tian, J. Liu, Z. Wu, S. Cui, J. Ding, Z. Dai and W. Wu, *J. Mater. Chem. C*, 2016,
- 619 4, 6327-6335.
- 620 37. R. E. Rojas-Hernandez, F. Rubio-Marcos, A. Serrano, I. Hussainova and J. F. Fernandez, *J.*
- 621 *Eur. Ceram. Soc.*, 2020, 40, 1677-1683.
- 622 38. J. Park, K. Park, J. Lee, J. Kim, S. M. Kim and P. Kung, *Jpn. J. Appl. Phys.*, 2010, 49, 042603.
- 623 39. F. K. Lotgering, *J. Inorg. Nucl. Chem.*, 1959, 9, 113-123.
- 624 40. U. Holzwarth and N. Gibson, *Nat. Nanotechnol.*, 2011, 6, 534.
- 625 41. Feldbach, E. Töldsepp, M. Kirm, A. Lushchik, K. Mizohata and J. Räisänen, *Opt. Mater.*, 2016,
- 626 55, 164-167.
- 627 42. V. Pankratov, R. Pärna, M. Kirm, V. Nagirnyi, E. Nömmiste, S. Omelkov, S. Vielhauer, K.
- 628 Chernenko, L. Reisberg, P. Turunen, A. Kivimäki, E. Kukk, M. Valden and M. Huttula, *Radiat.*
- 629 *Meas.*, 2019, 121, 91-98.
- 630 43. R. Pärna, R. Sankari, E. Kukk, E. Nömmiste, M. Valden, M. Lastusaari, K. Kooser, K. Kokko,
- 631 M. Hirsimäki, S. Urpelainen, P. Turunen, A. Kivimäki, V. Pankratov, L. Reisberg, F. Hennies,
- 632 H. Tarawneh, R. Nyholm and M. Huttula, *Nucl. Instrum. Methods Phys. Res.*, 2017, 859, 83-
- 633 89.
- 634 44. M. Masjedi-Arani and M. Salavati-Niasari, *Ultrason. Sonochem.*, 2016, 29, 226-235.
- 635 45. G. Hu, W. Li, G. He, J. Wang, Y. Zhao, Y. Zhang and B. Yao, *Ceram. Int.*, 2016, 42, 7852-
- 636 7856.
- 637 46. H. Chen, G. Wang, L. Zhao, X. He, C. Huang, W. Li, W. Fang and X. Du, *Microporous*
- 638 *Mesoporous Mater.*, 2017, 243, 331-338.
- 639 47. L. Li, A. Fijneman, J. Kaandorp, J. Aizenberg and W. Noorduyn, *Proc. Natl. Acad. Sci. U. S.*
- 640 *A.*, 2018, 115, 3575.
- 641 48. W. Li, C. Xu, A. Xie, K. Chen, Y. Yang, L. Liu and S. Zhu, *Crystals*, 2021, 11, 1481.
- 642 49. J. F. Scott and S. P. S. Porto, *Phys. Rev.*, 1967, 161, 903-910.
- 643 50. J. Etchepare, M. Merian and P. Kaplan, *J. Chem. Phys.*, 1978, 68, 1531-1537.
- 644 51. N. S. Bekturganov, M. R. Bissengaliyeva and D. B. Gogol, *Eurasian Chem. Technol. J.*, 2013,
- 645 15, 227.
- 646 52. M. Czaja, R. Lisiecki, R. Juroszek and T. Krzykowski, *Minerals*, 2021, 11, 1215.
- 647 53. H. Ji, Z. Huang, Z. Xia, M. S. Molochev, V. V. Atuchin, M. Fang and S. Huang, *Inorg. Chem.*,
- 648 2014, 53, 5129-5135.
- 649 54. W. Sun, T. Shi, L. Luo, X. Chen, P. Lv, Y. Lv, Y. Zhuang, J. Zhu, G. Liu, X. Chen and H.
- 650 Chen, *Adv. Mater.*, 2019, 31, 1808024.
- 651 55. N. Rakov, F. Matias, Y. Xing and G. S. Maciel, *Opt. Mater.: X*, 2024, 24, 100359.
- 652 56. X. Jiang, X. Gao, L. Li, P. Zhou, S. Wang, T. Liu, J. Zhou, H. Zhang, K. Huang, Y. Li and M.
- 653 Wang, *ACS Appl. Mater. Interfaces*, 2023, 17, 21228-38.
- 654 57. C. Baratto, E. Comini, M. Ferroni, G. Faglia and G. Sberveglieri, *CrystEngComm*, 2013, 15,
- 655 7981-7986.



- 656 58. H. He, Y. Wang and Y. Zou, *J. Phys. D Appl. Phys.*, 2003, 36, 2972.  
657 59. H. J. Chang, H. D. Park, K. S. Sohn and J. D. Lee, *J. Korean Phys. Soc.*, 1999, 34, 545-548.  
658 60. V. S. Kortov, K. A. Sergeeva, V. A. Pustovarov and A. A. Rempel, *J. Surf. Invest. X-Ray,*  
659 *Synchrotron Neutron Tech.*, 2017, 11, 727-731.  
660 61. Spassky, V. Mikhailin, M. Nazarov, M. N. Ahmad-Fauzi and A. Zhbanov, *J. Lumin.*, 2012,  
661 132, 2753-2762.  
662 62. E. N. Bunting, *J. Am. Ceram. Soc.*, 1930, 13, 5-10.  
663 63. L. Xia, Z. Liu and P. A. Taskinen, *J. Eur. Ceram. Soc.*, 2015, 35, 4005-4010.

View Article Online  
DOI: 10.1039/D6TC00560H



# Molten Salt–Assisted Screen Printing of Highly Textured $\text{Zn}_2\text{SiO}_4$ Films with Enhanced Deep UV Emission

Jallouli Necib\*<sup>1</sup>, Eduard Feldbach<sup>2</sup>, Ivo Romet<sup>2</sup>, Vitali Nagirnyi<sup>2</sup>, Irina Hussainova<sup>1</sup>, Thomas Jüstel<sup>3</sup>, and Rocío E. Rojas-Hernandez<sup>1,4</sup>

<sup>1</sup> Department of Mechanical and Industrial Engineering, Tallinn University of Technology, Ehitajate 5, 19180 Tallinn, Estonia

<sup>2</sup> Institute of Physics, University of Tartu, W. Ostwald Str 1, 50411 Tartu, Estonia

<sup>3</sup> FH Münster University of Applied Sciences, Department of Chemical Engineering, Stegerwaldstr. 39, D-48565, Steinfurt, Germany

<sup>4</sup> Electroceramic Department, Instituto de Cerámica y Vidrio, CSIC, Kelsen 5, 28049, Madrid, Spain

## Data Availability Statement

Data for this article, including raw XRD patterns, SEM images, cathodoluminescence spectra, and X-ray excited optical luminescence spectra, are available at the TalTech Data Repository at <https://doi.org/10.48726/qgpyv-k5q16>.

Supplementary information (SI) containing additional cross-sectional SEM micrographs demonstrating film thickness and interface morphology across different processing temperatures and compositions.

